A Modeling Study of Typhoon Lekima (2019) with the Topographic Influence of Taiwan

CHING-YUANG HUANG,[a] SHENG-HAO SHA,[a] AND HUNG-CHI KUO[b]

[a] *Department of Atmospheric Sciences, National Central University, Jhongli, Taiwan*
[b] *Department of Atmospheric Sciences, National Taiwan University, Taipei, Taiwan*

(Manuscript received 13 July 2021, in final form 14 April 2022)

ABSTRACT: The global model FV3GFS is used to simulate Typhoon Lekima (2019), which exhibited track deflection when approaching west-northwestward toward Taiwan. The model successfully simulates the observed northward deflection and the track deflection is produced by topographically induced wavenumber-1 flow with a pair of vorticity gyres around the typhoon center. The gyres tend to rotate counterclockwise about the typhoon center and thus induce an earlier northward and then westward movement. Azimuthal-mean kinetic energy budget of the typhoon indicates that the effect of Taiwan terrain modifies the correlation between the recirculating flow and pressure gradient force east of Taiwan, leading to a slight weakening of the typhoon during the later track deflection. The northward cyclonic deflection in general will be induced for a cyclone to move toward the central to northern terrain such as Lekima. The curvature of the northward cyclonic deflection, however, is large (small) for a northwestbound (nearly westbound) vortex depending on the track-topography-impinging angle. The curvature difference can be explained with the concept of recirculating flow, which is the flow splitting due to topography and rejoins the vortex to produce the wavenumber-1 asymmetry. The cyclonic track curvature of the northwestbound Lekima is larger than that of the westbound Maria (2018) in the FV3GFS simulations. This adds robustness to the conclusion that minor to moderate terrain-related track deflections can be well simulated by the FV3GFS global model near Taiwan.

KEYWORDS: Idealized models; Numerical analysis/modeling; Numerical weather prediction/forecasting

1. Introduction

Large impacts of topographic influences on translational tropical cyclones have been well documented in the literature, in particular, for an isolated high mountain, the Central Mountain Range (CMR) over 3000-m height in Taiwan (Wu and Kuo 1999). Translating tropical cyclones past the CMR or similar mountain terrain have been widely investigated, but mainly focused on TCs with landfall at the terrain (e.g., Jian and Wu 2008; Lin and Savage 2011; Huang et al. 2011; Chien and Kuo 2011; Hsu et al. 2013, 2018; Wu et al. 2015; Tang and Chan 2016a,b; Huang et al. 2016a,b, 2019, 2020b; Lin et al. 2016; Huang and Wu 2018). Most impinging typhoons for investigation move toward the main body of the mountain. In this case, topographical effects not only can modulate the core structure of the cyclone but also change the environmental flow that steers the cyclone. Most of the typhoons were moving westward and associated with appreciable track variations (e.g., Chang et al. 2013) in response to the strong blocking effect of the mountain terrain.

In the past 50 years, a few of TCs moved westward or northwestward offshore toward northern Taiwan with northward track deflection, including Nelson (1985), Sinlaku (2002), Wipha (2007), Trami (2013), Maria (2018), and Lekima (2019) (see Huang et al. 2020b). The recent Typhoon Hagupit in August 2020 also exhibited a similar northwestward track of Lekima with northward deflection northeast offshore of northern Taiwan. The northward deflection associated with the west-northwestward track of Maria (2018) that passed at an offshore distance of about 150 km from northern Taiwan at quasi-stationary intensity has been investigated using the global variable-resolution FV3-based GFS, i.e., FV3GFS (Huang et al. 2020b). The northwestward Lekima (2019) once reached the rapid intensification (RI) (Kaplan and DeMaria 2003) prior to the track deflection according to the CWB best track data (Shi and Chen 2021). Lekima is somewhat stronger than Maria, with a deflected track farther offshore about 250 km away from northern Taiwan. There is no direct simulation to verify whether such an observed track deflection can be induced by topographic effects and to understand the dominant dynamic processes causing the deflection.

The complicated situations associated with different impinging typhoons have been simplified and investigated by idealized numerical models. Systematic numerical experiments indicate that upstream track deflection of westbound cyclones toward the central mountain range can be controlled by the factor R/L_y where R is the radius of the maximum tangential wind of the initial vortex and L_y the mountain length scale in the direction normal to the vortex movement) (Lin et al. 1999, 2002, 2005; Huang et al. 2016a). Since most of the terrain effect arises to influence the typhoon movement as stronger northerly flow in the midtroposphere is induced by channeling effects ahead of the mountain (e.g., Wu et al. 2015; Huang et al. 2016a; Huang and Wu 2018), the controlling parameter is applicable to the terrain–typhoon configuration to a large extent. However, the parameter does not take into account the

Denotes content that is immediately available upon publication as open access.

Corresponding author: Ching-Yuang Huang, hcy@atm.ncu.edu.tw

DOI: 10.1175/MWR-D-21-0183.1

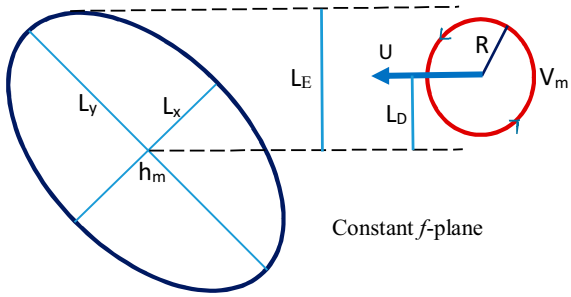

U: Basic flow speed
V_m: Vortex maximum wind speed
R: Radius of maximum wind
L_E: Effective terrain scale perpendicular to basic flow
L_D: Meridional departure distance of the vortex
L_x: Half width of the short terrain axis
L_y: Half width of the long terrain axis
h_m: Maximum terrain height

FIG. 1. Schematic diagram of a translational vortex (with maximum wind speed of V_m at the radius of R) at basic wind of U toward an elliptical mountain range at a maximum height of h_m on constant f plane. L_E is the effective projection of the terrain length perpendicular to mean wind. L_D is the meridional departure of the vortex center from the latitude of the central terrain peak. L_x and L_y are the terrain half widths of the two orthogonal axes, respectively. L_D is positive (negative) for a translational vortex departing north (south) of the terrain center.

initial meridional departure distance of a vortex and the orientation of an elliptical mountain range as shown in Fig. 1 that depicts the generalized configurations of the incident vortex and mountain range. In this example, the shorter and longer radii of the mountain range are defined as L_x and L_y, respectively. For a vortex moving westward at a speed of U, a meridional departure distance L_D (relative to the latitude of the mountain peak) needs to be considered since it is also related to the degree of flow blocking or splitting. The length scale L_y of the mountain range may be reduced when it is oriented at a tilting angle from the north, herein called the effective terrain scale L_E in the direction perpendicular to the basic flow. Accordingly, L_E will be equal to L_x for intercepting the impinging vortex as the long-axis is parallel to the basic flow. Therefore, there are varying landfall points, meridional departure distances, and terrain orientation angles, widening the spectrum of track behaviors of an incident cyclone moving toward a mountain range.

For constant f, this idealized prototype can be applied to the emulation of different incident typhoons toward the CMR by the specification of the tilting angle. Larger L_D, either rightward or leftward, tends to produce a rightward deflection ahead of the mountain range for a large R/L_E (Huang et al. 2016a; Huang and Wu 2018). Based on systematic experiments with an idealized regional model, the track deflection mechanisms have been investigated for TCs moving northwestward offshore around northern Taiwan (Tang and Chan 2016a,b). Idealized WRF simulations have been used to

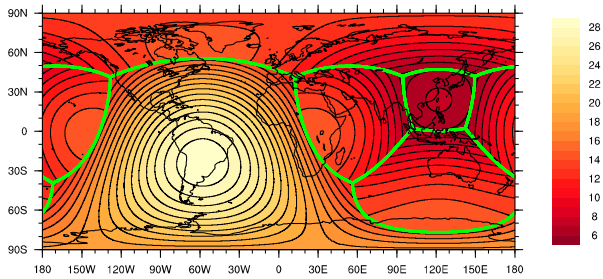

FIG. 2. The cubed-sphere simulation domain of FV3GFS for the experiments with the highest stretched resolution of about 7 km in the vicinity of Taiwan. Shaded colors and contours (with an interval of 2 km) indicate the horizontal resolution.

emulate the observed track deflection of tropical cyclones past a mesoscale mountain (e.g., Huang et al. 2020b).

This paper is organized as below. Numerical aspects are given in section 2 to introduce the global model and real-case experiments conducted in this study. Simulated results of the experiments with FV3GFS are presented and compared with the observations in section 3. The evolving typhoon structure and associated transverse circulation are presented with a focus on the topographic influence of Taiwan terrain on Lekima's track deflection. Azimuthal-mean kinetic energy (KE) budget analyses of the typhoon near track deflection are performed to understand the major contributions of mean (symmetric) flow and eddy (asymmetric) flow to the cyclone's intensity change at later stages of RI. In section 3, a brief summary regarding the roles of the parameters L_D and L_E is given to compare the contracting tracks between Maria and Lekima that moved toward northern Taiwan but in different directions, based on FV3GFS simulations and idealized simulations. Finally, conclusions are given in section 4.

2. Numerical aspects

a. *The global model and numerical experiments*

The global model FV3GFS applied to simulate Typhoon Lekima in this study is the same as in Huang et al. (2020b) that provides a more detailed introduction. FV3GFS is a nonhydrostatic model consisting of the finite-volume cubed sphere dynamic core (FV3) and the Global Forecast System (GFS) physics packages and has been implemented into the Next Generation Global Prediction System (NGGPS) at the National Centers for Environmental Prediction (NCEP) for global operational forecast. The cubed sphere of FV3GFS allows for the removal of the singular polar point possessed by a global spectral model (Putman and Lin 2007). For FV3GFS, enhanced global horizontal resolution by enabling nested specific faces as well as stretching the cubed sphere can be used in any targeted face of interest to improve forecasts with higher resolution (e.g., Harris et al. 2016; Hazelton et al. 2018a,b; Zhou et al. 2019). The regular cubed spheres of FV3 with 768 × 768 grids in each cube are featured with stretched grids that gradually enhance the horizontal grid spacing to about 7 km near the central region of the targeted face as shown in Fig. 2. For Typhoon Lekima moving near offshore

TABLE 1. Numerical experiments with different physics schemes. The GFDL cloud microphysics scheme is a single-moment scheme of six hydrometeor species based on Lin et al. (1983). WSM6 is the WRF single-moment 6-class scheme. The 2010 deep convection scheme is a simplified Arakawa–Schubert (SAS) scheme called old SAS. Afterward, it was upgraded as new SAS.

Expt	Cloud microphysics	Shallow convection	Deep convection
CTL	GFDL	Scale and aerosol-aware	Scale and aerosol-aware
THOM	Double-moment (Thompson)	Scale and aerosol-aware	Scale and aerosol-aware
WSM6	Single-moment (WSM6)	Scale and aerosol-aware	Scale and aerosol-aware
S_MF	GFDL	Jul 2010 mass flux	Scale and aerosol-aware
Tied	GFDL	Modified Tiedtke's eddy diffusion	Scale and aerosol-aware
NSAS	GFDL	Scale and aerosol-aware	Jul 2010 SAS
OSAS	GFDL	Scale and aerosol-aware	Before Jul 2010 SAS

of northern Taiwan, grid stretching centered at 24°N, 121°E (central Taiwan) is employed in this study.

For the control experiment (denoted by CTL) in this study, the Geophysical Fluid Dynamics Laboratory (GFDL) cloud microphysics scheme is used. The GFDL cloud scheme is a single-moment scheme of six hydrometeor species based on Lin et al. (1983). All the experiments use a total of 64 vertical layers in a hybrid-pressure terrain-following coordinate with a model top of 1 hPa. For the initial condition of FV3GFS, the NCEP Global Data Assimilation System (GDAS) reanalysis data at a horizontal resolution of 0.25° × 0.25° are used. To investigate the topographic influence of Taiwan terrain, the whole Taiwan island is completely reset to the ocean in an experiment (denoted by noTW). Several experiments were conducted to explore the sensitivity of FV3GFS performances to physical parameterization schemes used in the simulations, as listed in Table 1. The physics schemes include cloud microphysics schemes, a partial double-moment Thompson scheme (denoted by THOM) and WRF single-moment 6-class scheme (WSM6), and cumulus parameterization schemes, the July 2010 version of mass-flux shallow convection scheme (S_MF) and the modified Tiedtke convection scheme (Tied), and the new July 2010 version of simplified Arakawa–Schubert (SAS) convection scheme (NSAS) and old SAS convection scheme (OSAS); for the physics schemes, related references can be found in Huang et al. (2020b). For all conducted experiments, the sea surface temperature from NCEP GDAS is unchanged during the model integration of a total of 120 h.

b. *Azimuthal-mean kinetic energy budget*

Azimuthal-mean kinetic energy (KE) budget terms in cylindrical coordinates are analyzed in this study to understand the dynamic processes contributing to the intensity evolution of the typhoon moving near the terrain. The governing equation of azimuthal-mean KE tendency is derived in the appendix where various KE budget terms are described.

3. FV3GFS simulation results of Lekima

a. *Typhoon forecasts and sensitivities to physics schemes*

The simulated tracks for CTL and the best track of the Japan Meteorological Agency (JMA), as well as the evolutions of their maximum typhoon wind speed (V_{max}) and minimum sea level pressure (MSLP) from 1200 UTC 6 August 2019 (the initial time of model simulations), are shown in Fig. 3. Results of the other six sensitivity experiments using different physics schemes in Table 1 are also shown in this figure. Most of the global and regional operational models did not capture Lekima's track deflection in their forecasts at this model initial time (the forecasted tracks are available from http://www.typhoon2000.ph/multi/log.php?name=LEKIMA_2019, and https://www.emc.ncep.noaa.gov/gc_wmb/vxt/HWRF/tcall.php). Some of the forecasted tracks even made landfall at Taiwan. The FV3GFS also gave a somewhat southward track deviation in the forecasts at earlier model initial times (figures not shown). The simulated tracks for all the experiments in Fig. 3a, in general, do not deviate considerably from the best track, particularly prior to the observed track deflection near 0000 UTC 8 August 2019, while the track errors increase faster afterward as the typhoon turns northward. The tracks are sensitive to use of the physics schemes near the track deflection stage despite the fact that the associated intensity forecasts are not much different. As shown in Fig. 3b, both CTL and OSAS experiments have better captured the observed track deflection among the experiments; such northward track deflection disappears as the Taiwan terrain is set to the ocean in their terrain-denial experiments, noTW and OSAS_noTW, respectively. The track deflection commences from about 42 h and rebounds back near 66–72 h.

For both CTL and OSAS, the simulated V_{max} and MSLP follow the best track intensities quite well by 80 h (forecast time), although somewhat underpredicted before the peak intensity stage. For CTL, there is a slight weakening of the typhoon intensity in 51–54 h just before the deflection is largest near 54 h, but it is slightly stronger at 57 h for noTW. The later forecasts after 80 h with well-maintained and stronger intensity appear to largely deviate from the observed, likely due to their offshore biased tracks without the observed landfall. Such increased track deviations for CTL could also be attributed to the simulated weaker mid-latitudinal ridge to the north of the typhoon, compared to the corresponding NCEP GDAS reanalysis (figures not shown). CTL obtains a slightly closer intensity forecast than OSAS when both are compared with the best track results. Thus, the results from the CTL experiment are used

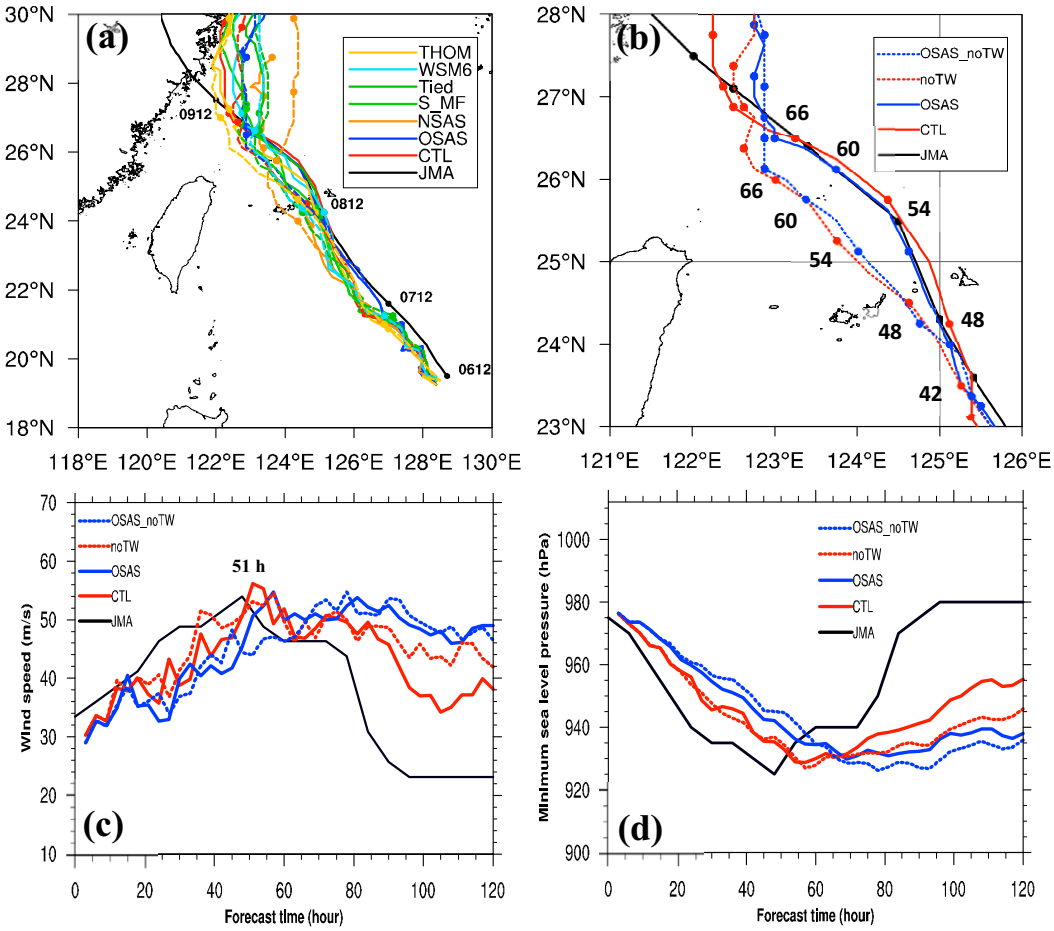

FIG. 3. (a) Simulated tracks of total 120 h for 6 physics-sensitivity experiments and the control experiment CTL (solid: with the Taiwan terrain; dashed: without the Taiwan terrain) and the best track of JMA (black solid) from 1200 UTC 6 Aug 2019. (b) As in (a), but for the experiments with Taiwan terrain (in solid) for CTL (red) and OSAS (blue), and their sensitivity experiments without Taiwan terrain for noTW and OSAS_noTW (dashed), respectively. (c) Time evolution of simulated 10-m maximum wind speed (m s^{-1}) of the typhoon for CTL (solid red) and OSAS (solid blue) and their terrain-denial experiments noTW (dashed red) and OSAS_noTW (dashed blue) as well as the best track intensity of JMA (black). (d) As in (c), but for minimum sea level pressure (hPa). For CTL, the largest *V*max appears at 51 h as indicated in (c).

for further dynamic analyses on track deflection and intensity evolution in later sections.

b. *Typhoon primary circulation*

The simulated typhoons at 850 hPa for CTL and noTW (CTL without the Taiwan terrain) are shown in Fig. 4 at 42, 48, and 54 h when the typhoon is at the early deflection stage. For comparison, the results at 48 h for OSAS and OSAS_noTW (OSAS without the Taiwan terrain) are also shown in the figure. At 42 h, the typhoon's circulations for both CTL and noTW (Figs. 4a,e) are similar, except for the Taiwan area with the stronger outer skirting flow passing over the Taiwan terrain for the latter. The typhoon outer flow becomes split ahead of northern Taiwan at a later time (48 h) and its left (eastern) branch tends to rejoin the inner vortex core to the southwest of the vortex center. The right branch keeps moving southwestward and then passes around the southern end of Taiwan to converge with the southerly southwesterly flow south of the inner typhoon (Figs. 4b,f). The flow convergence thus is significantly intensified mainly at the southeast quadrant of the typhoon. At this time (48 h), the simulated typhoon has started to deflect northward. This asymmetric radial flow with a stronger southerly wind component is further intensified at 54 h, thus driving the typhoon more northward compared to noTW (Figs. 4c,g). The intensification of the asymmetric flow is also evident at upper levels, e.g., 500 hPa (figures not shown). Compared to CTL, OSAS also shows similar flow intensification mainly at the southeast quadrant, for example, at 48 h (Figs. 4d,h). Both experiments produce quite similar tracks with comparable deflection since their typhoon structures and intensities are only slightly varied. Both experiments substantiate

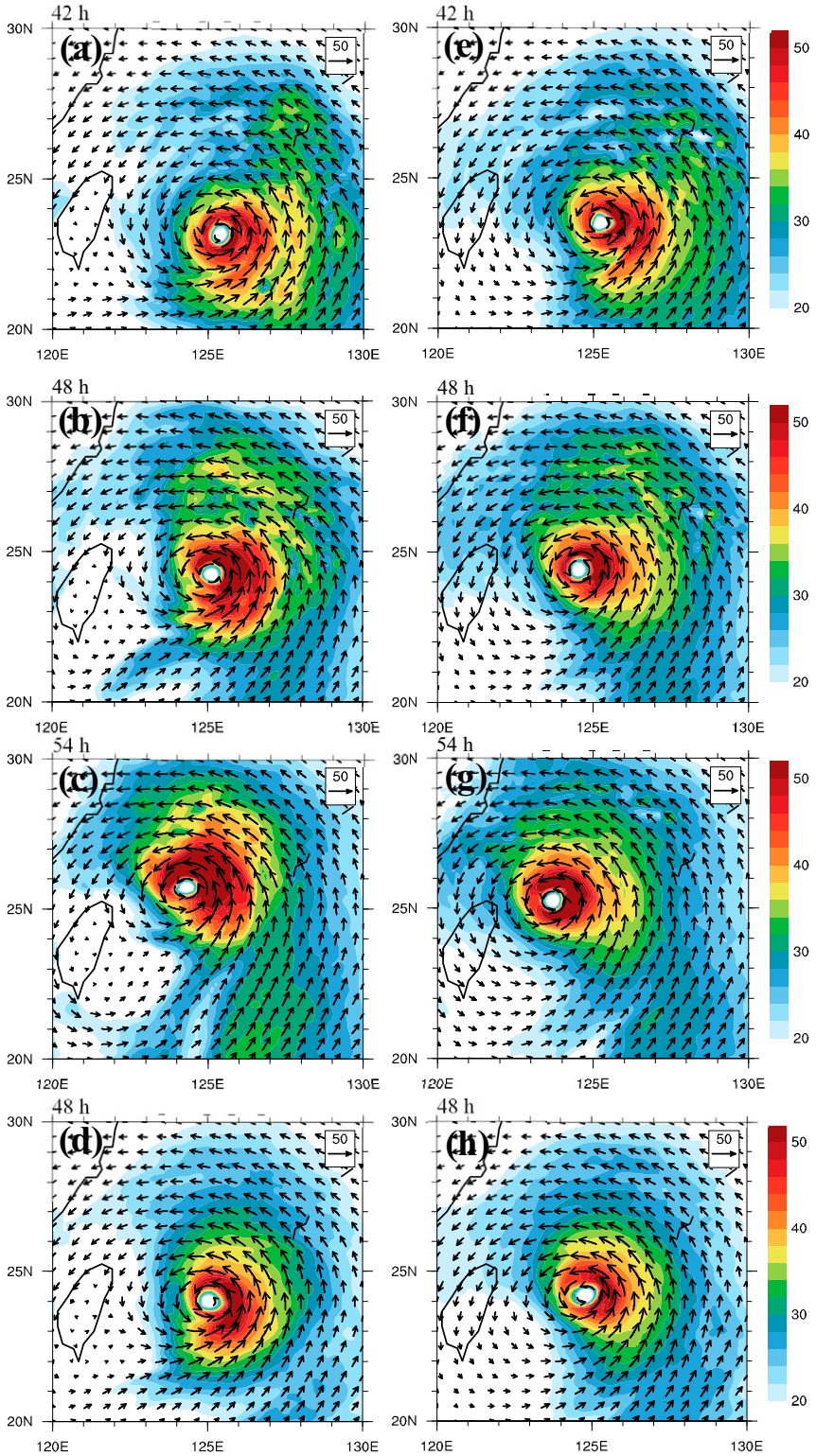

FIG. 4. Simulated horizontal wind vectors at 850 hPa (shaded colors m s^{-1}) for CTL at (a) 42, (b) 48, and (c) 54 h. (e)–(g) As in (a)–(c), respectively, but for noTW (as in CTL, but without the Taiwan terrain). (d) As in (b), but for OSAS. (h) As in (d), but for OSAS_noTW. A reference vector (m s^{-1}) is provided at the upper-right corner of each panel.

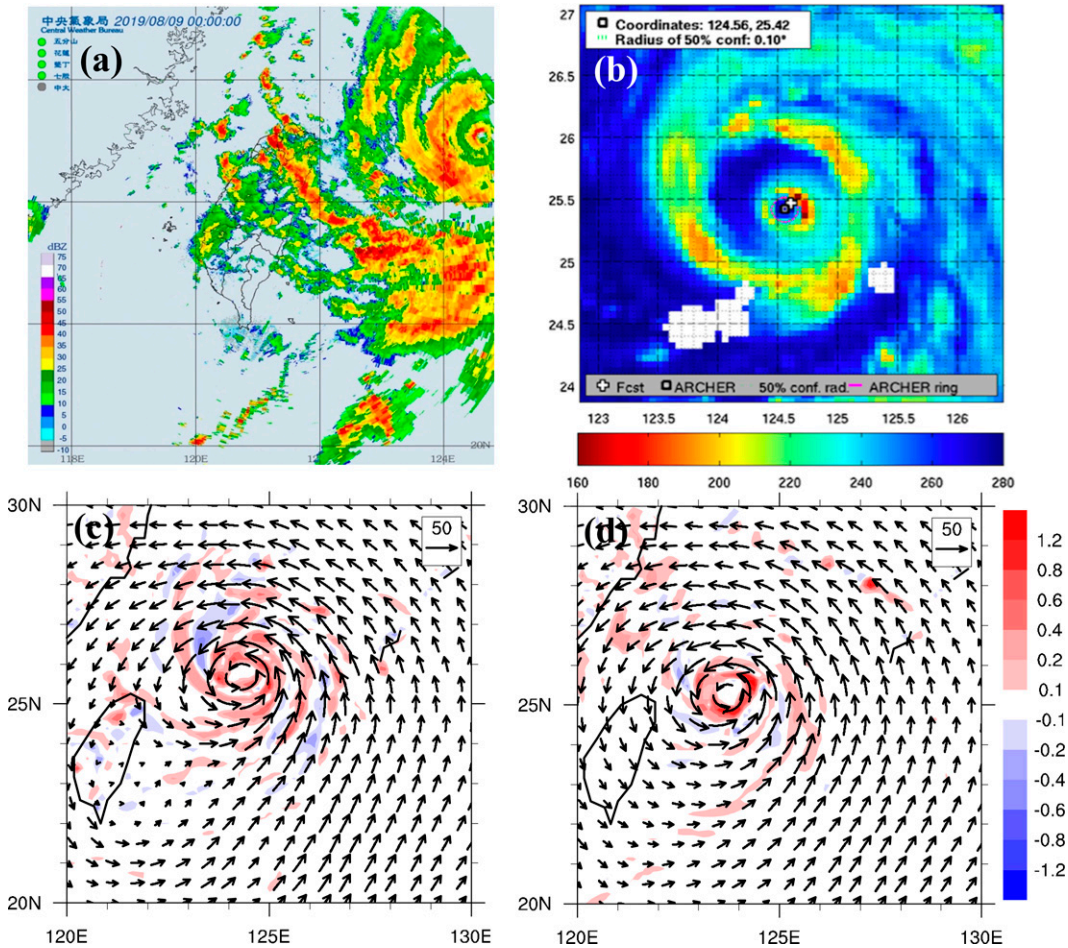

FIG. 5. (a) Observed radar reflectivity at 1600 UTC 8 Aug 2019 for Typhoon Lekima (available from CWB); (b) brightness temperature of Advanced Microwave Scanning Radiometer 2 at 1746 UTC 8 Aug 2019 for Typhoon Lekima (available from http://tropic.ssec.wisc.edu); (c) simulated horizontal wind (m s^{-1}) overlaid with vertical velocity (shaded colors; m s^{-1}) for CTL at 1.5-km height at 54 h (1800 UTC 8 Aug); and (d) as in (c), but for noTW.

the common fact that the Taiwan terrain produces a significant impact on the southern portion of the approaching Lekima. On the other hand, it was found that removal of the Taiwan terrain in other physics-sensitivity experiments (with weaker northward deflection) only leads to a small modification on the tracks. The track response to the impact of flow recirculating east of the Taiwan terrain is also similar to the west-northwestward-moving Maria (2018) that, however, approached closer to northern Taiwan with a less northward track deflection (Huang et al. 2020b). Realizing the involved complexity in the real global simulations, we thus apply an idealized regional model to verify the observed track deflection of Lekima in the FV3GFS simulations in section 4.

c. *Comparison with the observations for simulated convection*

Lekima indeed was accompanied by a concentric eyewall as it took the track deflection. Figure 5 compares the simulated vertical velocity at the 1.5-km height at 54 h for CTL and the observed radar reflectivity at 1600 UTC 8 August 2019 from CWB and bright temperature of Advanced Microwave Scanning Radiometer 2 (AMSR2) at 1746 UTC 8 August 2019. The CWB radar echoes (Fig. 5a) also well depict the left portion of the concentric eyewall that is fully discovered by the feature of lower cloud temperature from the satellite measurement (Fig. 5b). The simulated vertical motions for CTL have also exposed such a very narrow inner eyewall and an outer eyewall associated with spiral bands entailing outward. For noTW, the concentric eyewall structure is not clearly present (Fig. 5d). Without the enhanced recirculating flow east of Taiwan, the spiral convection is also significantly reduced at the southern flank of the inner typhoon. As shown in Fig. 3, the simulated Lekima is approaching its peak intensity near 51 h for CTL, afterward with a gradual decaying. Typhoons/hurricanes tend to cease their intensification or even become weakening once the concentric eyewall has formed (e.g., Willoughby et al. 1982; Black and Willoughby 1982; Terwey and Montgomery 2008). Note that the inner

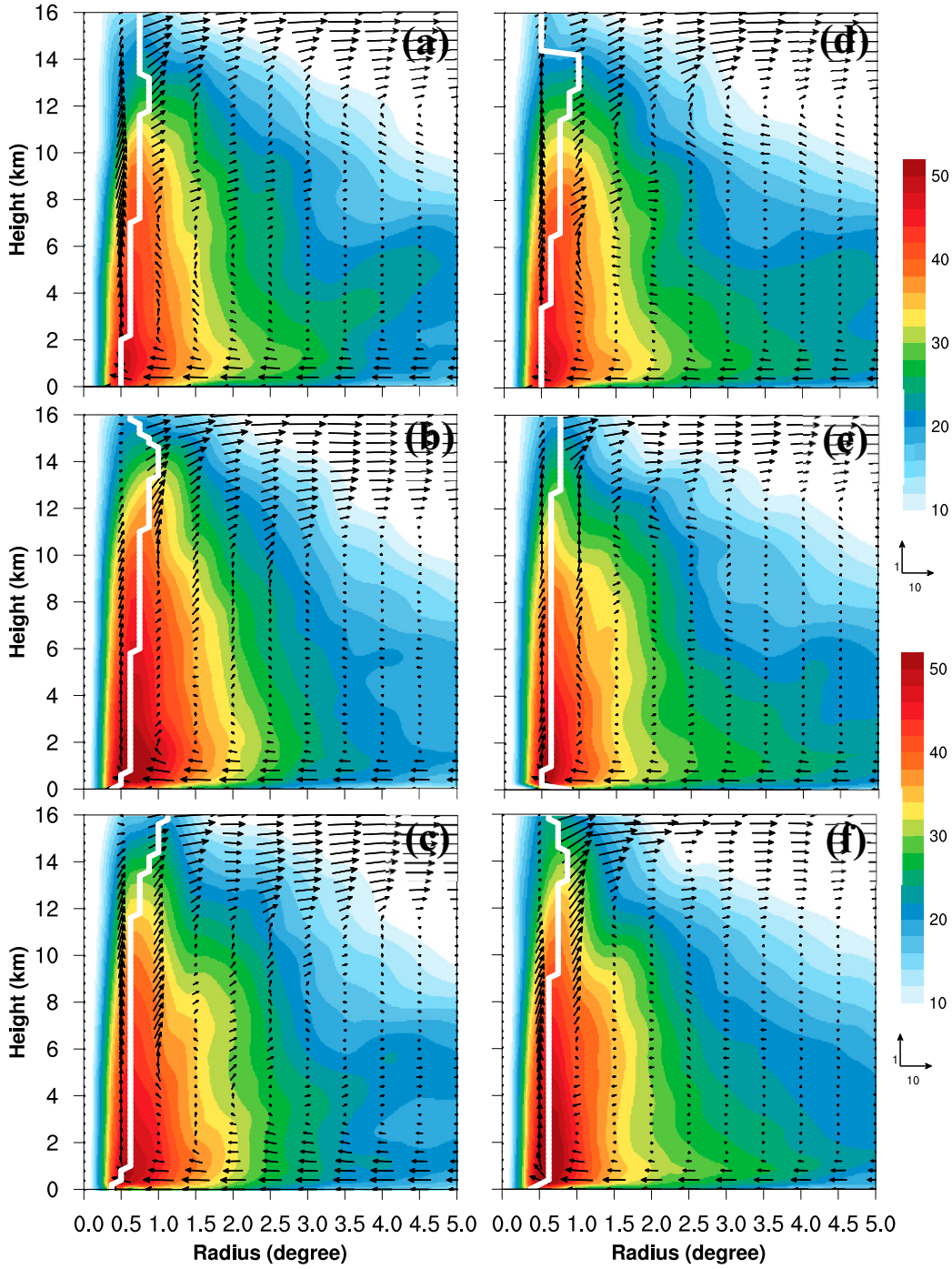

FIG. 6. Azimuthal-mean transverse circulation across the typhoon center for radial–vertical wind (vectors; m s^{-1}) and tangential wind speed (shaded colors; m s^{-1}) for CTL at (a) 42, (b) 48, and (c) 54 h. (d)–(f) As in (a)–(c), respectively, but for noTW. The radial and vertical wind scales (m s^{-1}) are indicated at the right. Connected white line segments indicate the radius of maximum wind speed. Scales of radial and vertical wind components (m s^{-1}) are indicated at the right column.

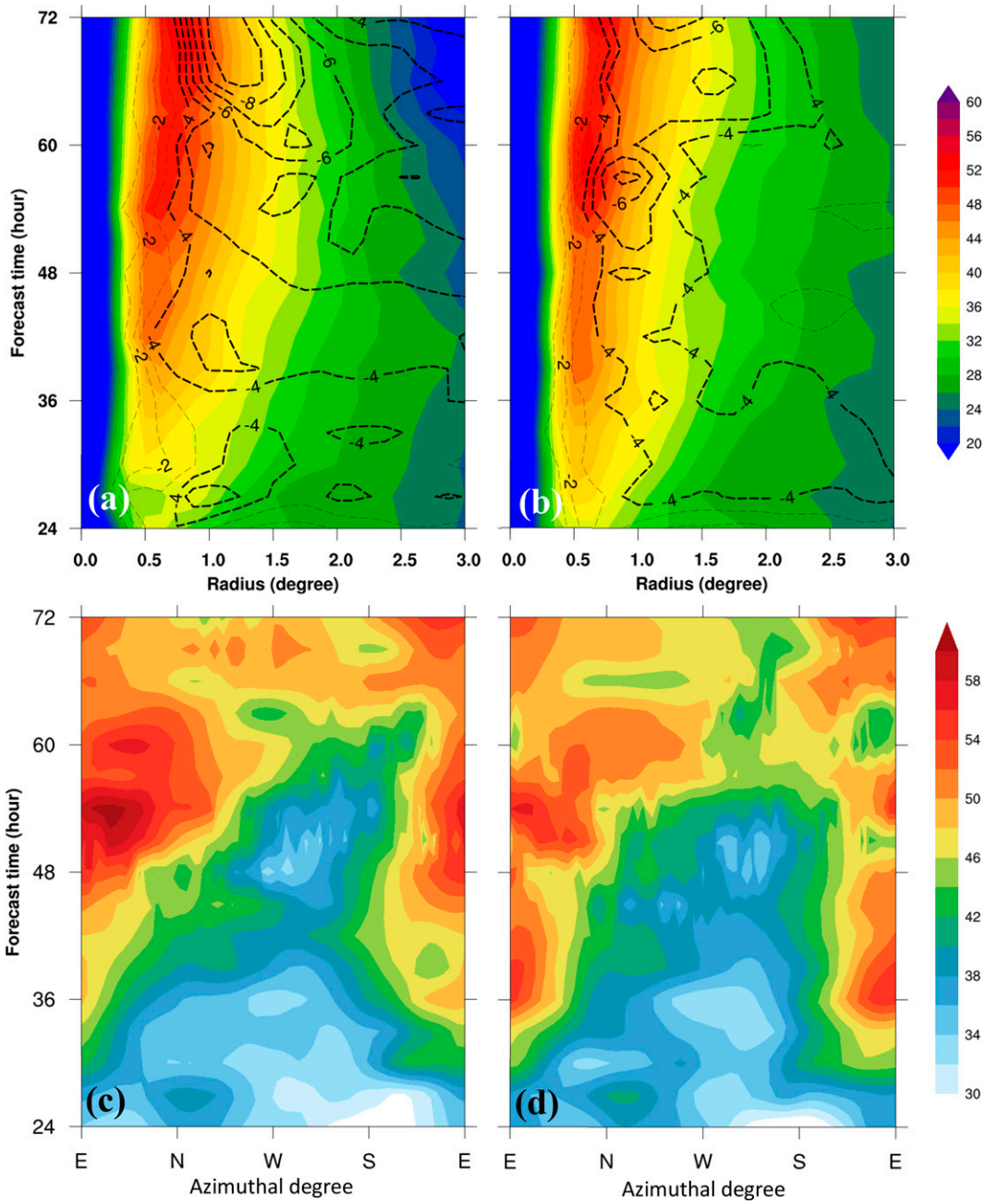

FIG. 7. Hovmöller plot of azimuthal-mean tangential wind speed (shaded colors; m s^{-1}) and radial velocity (contours with an interval of 1 m s^{-1}), averaged in 0–2-km height, with respect to radius (degrees) in 24–72 h for (a) CTL and (b) noTW. (c),(d) As in (a) and (b), respectively, but with respect to azimuthal variations of tangential wind speed averaged in 0–2-km height and the annulus of 0.5°–1°.

core of the simulated Lekima during the track deflection is still somewhat away from mainland China, and the slight weakening is not likely caused by the topographic effects of China terrain.

d. Typhoon transverse circulation

To further understand the difference in vertical development of the typhoons with and without the track deflection, Fig. 6 shows the azimuthal-mean transverse circulations across the typhoon center at 42, 48, and 54 h for CTL and noTW. At 42 h, the transverse circulations are similar for CTL and noTW, with the low-level inflow confined below about 2-km height and upper-level outflow above 11–12-km height. The tangential wind is well organized in the inner core (herein defined within the radius of 2.5°) with a radius of about 50 km for the maximum wind speed in the lower

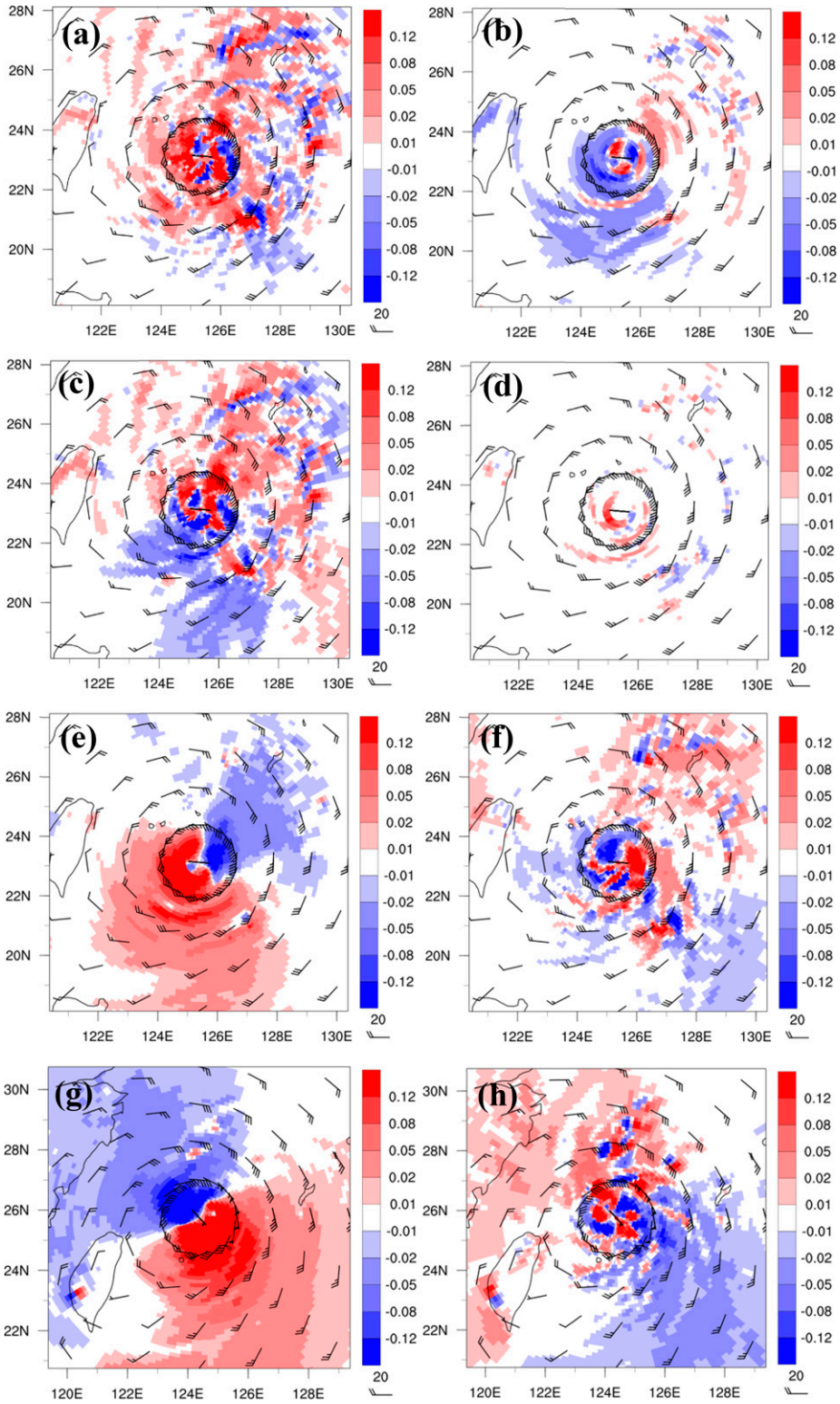

FIG. 8. The budget terms of kinetic energy (KE) (shaded colors in $10^{-3} \times m^2 s^{-3}$) averaged in 0–2-km height at 42 h for CTL overlaid with horizontal wind ($m\ s^{-1}$), shown for (a) sum of all budget terms, (b) radial KE advection, (c) tangential KE advection, (d) vertical KE advection, (e) work rate by radial pressure gradient force, and (f) work rate by tangential pressure gradient force. (g),(h) As in (e) and (f), respectively, but at 54 h.

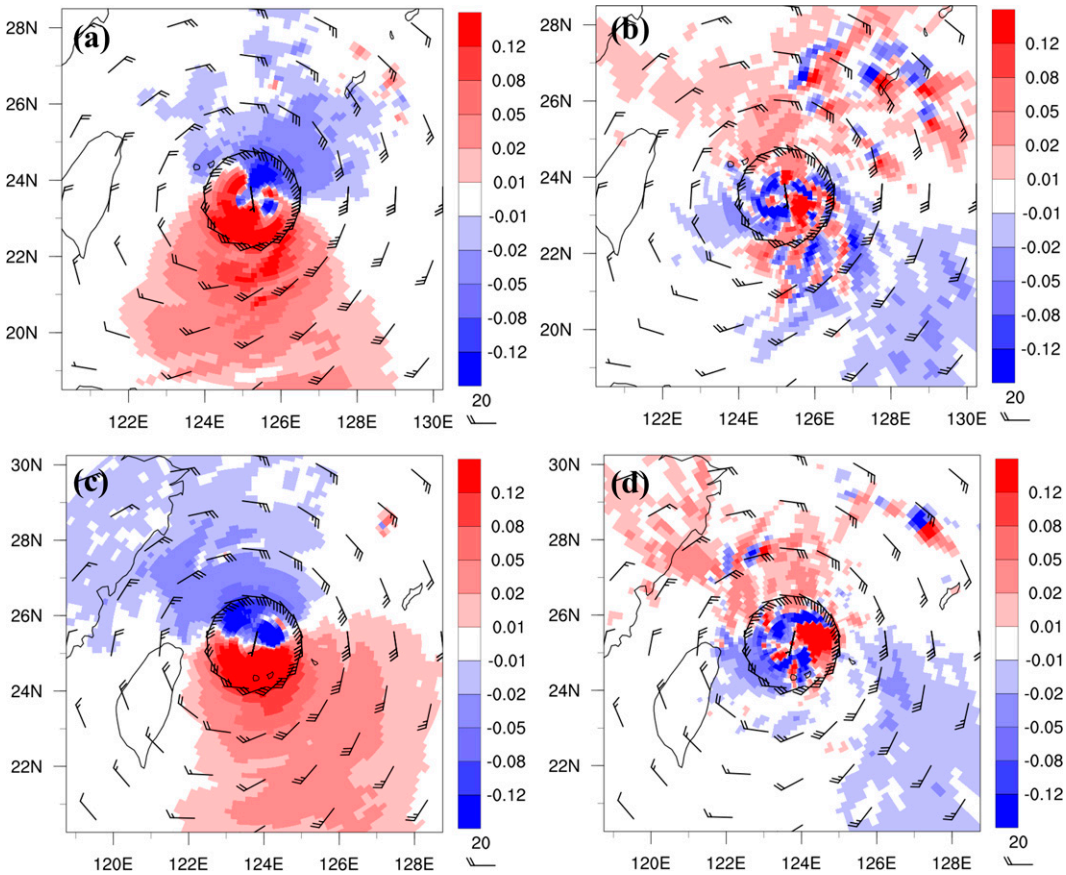

FIG. 9. The budget terms of kinetic energy (KE) (shaded colors; $\times 10^{-3}$ m^2 s^{-3}) averaged over 0–2-km height at 42 h for noTW overlaid with horizontal wind (m s^{-1}), shown for (a) work rate by radial pressure gradient forces and (b) work rate by tangential pressure gradient force. (c),(d) As in (a) and (b), respectively, but at 54 h.

troposphere (Figs. 6a,d). At 48 h, the azimuthal-mean transverse flow and primary flow are stronger and develop higher and farther out for CTL than noTW (Figs. 6b,e). The associated absolute angular momentum (AAM) is also slightly stronger for CTL (not shown). However, the primary vortex does not get more intense than noTW at 54 h, despite the fact that both inflow at low levels and outflow at upper levels at outer radii and middle levels near 2° are further enhanced for CTL. There is a slight increase of about 5 m s^{-1} in V_{max} near 51 h for CTL (Fig. 3c), but not identified in the azimuthal-mean primary circulation in the troposphere at 54 h (Figs. 6c,f). In the inner upper eyewall, both the azimuthal-mean tangential wind and AAM (not shown) are slightly weaker for CTL than noTW at this time.

The impact of the topographic effects on the track deflection is illustrated by Hovmöller plots in Fig. 7 that shows the time evolution of tangential and radial flow components averaged in 0–2-km height and the radii of 0.5°–1° from 24 to 72 h. The azimuthal-mean tangential flow structures are similar for both CTL and noTW during this period, except for a slightly outer expansion of the inner core (e.g., the contour for the tangential wind speed of 36 m s^{-1}) from about 42 to 66 h for the former (Figs. 7a,b). The topographic effects of the CMR indeed already exist before 42 h, with increasing influences on the typhoon from about 30 h. The radial flow has revealed more differences; for example, the inflow is considerably more intense outside the eyewall in the inner core after 36 h for CTL. A larger difference in both wind components as found after 60 h is related to their track deviations. The low-level tangential flow structures in the azimuth are quite similar by 36 h for both experiments (Figs. 7c,d), showing strong axisymmetry. A larger azimuthal difference in the tangential wind speed is present near 45–66 h when the track deflection is accompanied by a stronger-wind core rotating from the southeast, east, and then to the north. The greatest difference indeed is produced near 54 h when the track deflection is strongest, which is located near the northeast quadrant. Such a location of large tangential wind difference for CTL may facilitate the vortex to move northwestward near the time as seen in Fig. 3b.

e. *Kinetic energy budget*

In this study, we aim to investigate the evolution of the kinetic energy (KE) budget of Lekima since the simulated typhoon is associated with a strong intensification near the onset of track deflection and a slight weakening at the stage

of the strongest deflection as seen in Fig. 3. As shown in Fig. 6, the simulated Lekima, however, is affected by the CMR, with some differences in developed transverse circulations during the track deflection for CTL and noTW. We will identify the relatively more important contributions in the KE budget during the track deflection and the differences with and without the topographic influences.

The KE budget terms (see the appendix) averaged in 0–2-km height at 42 h are shown in Fig. 8. At the southern flank of the vortex, negative KE tendency is produced by the radial KE advection of the weaker flow southwest of the Taiwan terrain (Fig. 8b). Tangential KE advection also provides a negative contribution at the roughly same region and farther southern area, in response to the increasing flow speed along the circulation (Fig. 8c). Downwind of the accelerating flow, the KE tendency is mostly positive to enhance the flow east and north of the vortex center as shown in Fig. 4b. At this low level, vertical KE advection provides a rather small contribution to the KE tendency (Fig. 8d). The work rate done by radial pressure gradient force is more dominant and positive mainly west and south of the vortex center (Fig. 8e) and largely compensates for the KE loss by the horizontal (radial and tangential) advection. On the other hand, the positive KE input by tangential advection northeast of the vortex center in Fig. 8c is mainly consumed by the negative work rate by the outward radial flow correlated with positive radial pressure gradient force. In contrast, the work rate done by the tangential flow correlated with tangential pressure gradient force is much less organized with comparable magnitudes only in the inner vortex (Fig. 8f) where the correlation between the asymmetric flow and forcing is mostly positive and negative to the east and west of the vortex center, respectively. At 54 h, the positive work rate from the radial flow component is rotated counterclockwise by about 90° but counteracted by the increased negative contribution from the tangential flow component (Figs. 8g,h). The negative horizontal KE advection (in Figs. 8c,d) also follows the same rotation at this time (figures not shown). This mainly reflects that the region of radial inflow is shifting from south-southwest to south-southeast to supply with KE at this stronger-wind regime as shown in Fig. 4. Thus, the net KE budget at 42 h is mostly positive in the inner vortex with larger magnitudes to the south, despite some finer-scale irregular consumption (Fig. 8a); however, the net KE tendency at 54 h is mostly positive and is enhanced to the northeast of the vortex center (figures not shown) as the typhoon track is being deflected northward. The relative importance of the KE budget terms without the Taiwan terrain for noTW is similar to that for CTL at 42 h since both circulations show similar vortex intensities and sizes as seen in Fig. 6. For example, the geometric distributions of the KE tendency produced by radial and tangential pressure gradient forces at 42 h for noTW as shown in Fig. 9 are similar to those for CTL. However, the stronger positive and negative zones of these two terms that are rotating counterclockwise to the southeast and northwest of the vortex center at 54 h for CTL appear to be less rotated and present mainly to the south and north for noTW.

Bearing the geometric structure of the KE budget terms in mind, we present the azimuthal-mean of the KE budget terms computed from the decomposed mean (symmetric) and eddy (asymmetric) components of the vortex. There are 15 terms involved in the KE budget (excluding turbulent diffusion that is neglected in the analysis). Figure 10 shows nine more important budget terms at 42 h for CTL. Mean radial advection of mean KE (RMTKE) is mostly negative at the regions of the low-level inflow and eyewall and positive in the mid and upper-tropospheric outflow outside the radius of maximum wind (RMW) (Fig. 10b), while mean vertical advection of mean KE (VMTKE) is positively strong except for the inflow region near the surface (Fig. 10c). On the other hand, eddy radial advection of weighted radial momentum (ERRM) has no major contribution, except for in the upper eyewall with strong outflow (Fig. 10d), while eddy radial advection of weighted tangential momentum (ERTM) has distinguished negative and positive impacts inside and outside of the eyewall, respectively (Fig. 10e), contrasting the irregular moderate contribution from eddy tangential advection of weighted tangential momentum (EVTM) (Fig. 10f). The work rate by mean radial pressure gradient force (WMRP) provides the dominant positive contribution below about 6-km height in the inner core, above which negative effects are significant and widespread (Fig. 10g). Azimuthal-mean work rate by eddy radial pressure gradient force (WERP) delivers a somewhat positive tendency in the eyewall, but with a negative contribution outside the upper eyewall above about 8-km height (Fig. 10h). Finally, azimuthal-mean work rate by eddy tangential pressure gradient force (WETP) is mostly positive in the vortex with moderately larger magnitudes in the upper-level outflow (Fig. 10i), which indicates a general positive correlation between the local tangential flow velocity and tangential pressure gradient force in the inner vortex. The net outcome of these KE budget terms (TTKE) shown in Fig. 10 thus constitutes the positive KE tendency below about 6-km height in the inner core and negative KE tendency above this height near the eyewall (Fig. 10a). It appears that among the KE budget the WMRP term is the most dominant positive source in contribution to the vortex KE in the lower troposphere above which VMTKE also has a considerable positive impact. Relative contributions from the work-rate budget terms (WMRP, WERP, and WETP) at 42 h in CTL are not largely changed in noTW (Figs. 10j–l).

As the vortex is taking its strongest track deflection at 54 h, the KE budget terms exhibit somewhat different structural changes as shown in Fig. 11. Both mean advection terms (RMTKE and VMTKE) have contributed more positive tendency outside the RMW, particularly in the mid- to lower troposphere (Figs. 11b,c) than at 42 h. The earlier negative effect of ERTM has been reversed to positive contribution throughout the inner eyewall from 48 h to this time (Fig. 11e), while ERRM continues to have relatively minor effects (Fig. 11d). EVTM now gives more intense negative effects in the upper eyewall in response to the developing stronger outflow (Fig. 11f). The more dominant WMRP tends to greatly reduce the KE in the lower eyewall at this time (Fig. 11g). WERP appears to produce a wave structure at a radial wavelength of about 1.5° in the troposphere (Fig. 11h). The general positive source from WETP has changed signs with mostly negative impacts, except for the lowest 3 km near

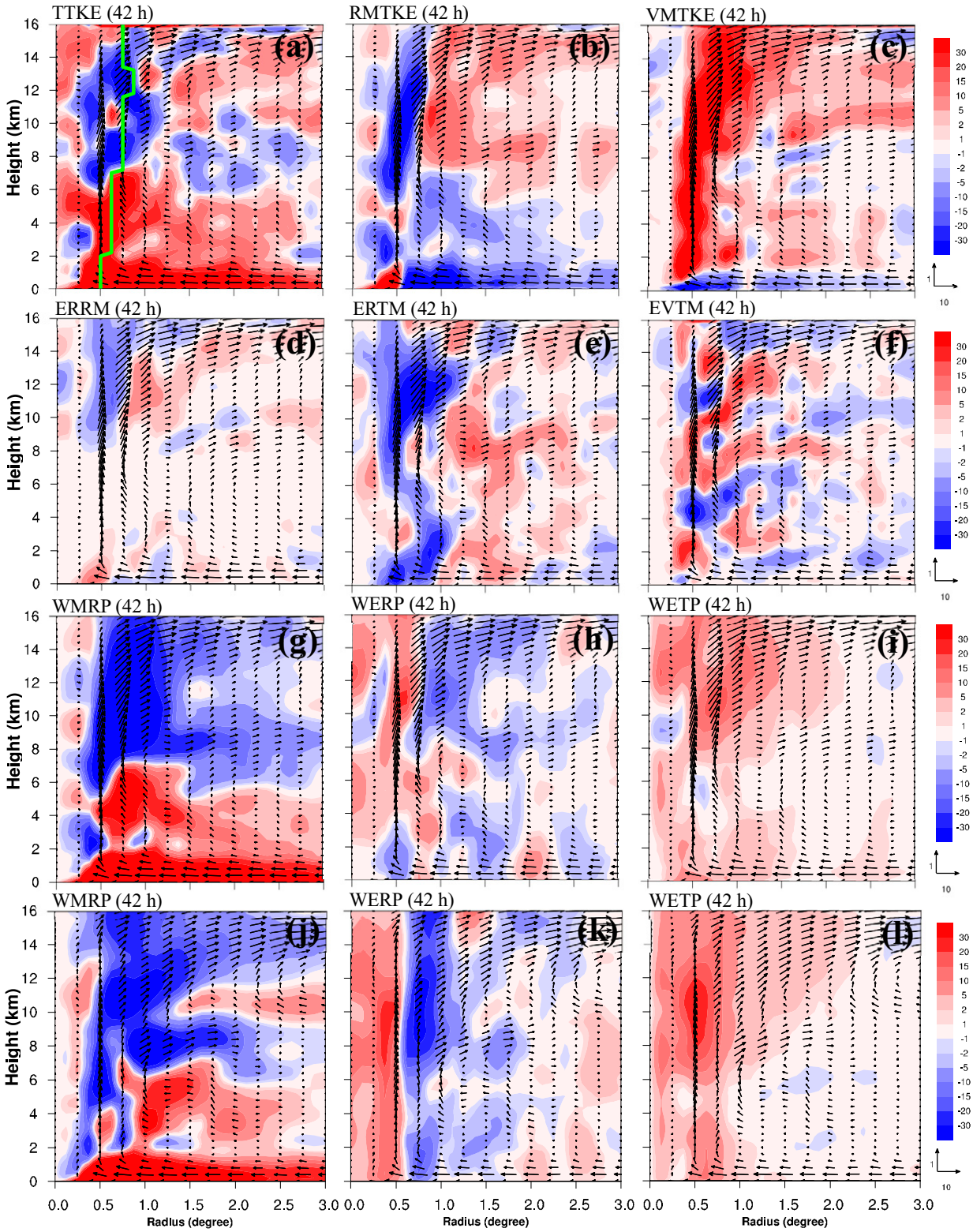

FIG. 10. The budget terms (shaded colors; $\times 10^{-3}$ m^2 s^{-3}) of azimuthal-mean kinetic energy (KE) overlaid with radial and vertical wind (m s^{-1}) at the height–radius cross section through the typhoon center at 42 h for CTL, shown for (a) TTKE, (b) RMTKE, (c) VMTKE, (d) ERRM, (e) ERTM, (f) EVTM, (g) WMRP, (h) WERP, and (i) WETP in the KE budget equation. (j)–(l) As in (g)–(i), respectively, but for noTW at 42 h.

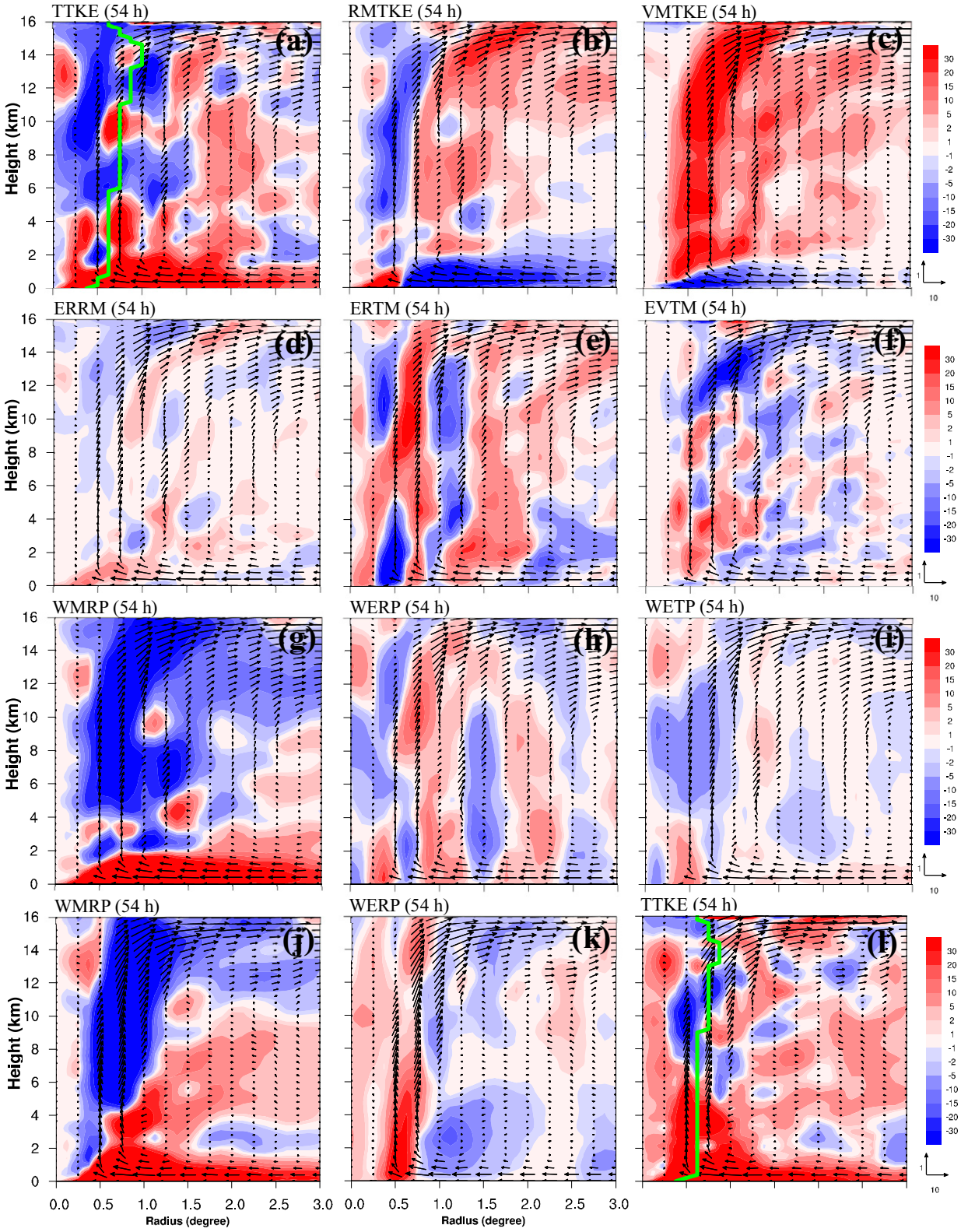

FIG. 11. As in Fig. 10, but at 54 h and (i) for TTKE at 54 h for noTW.

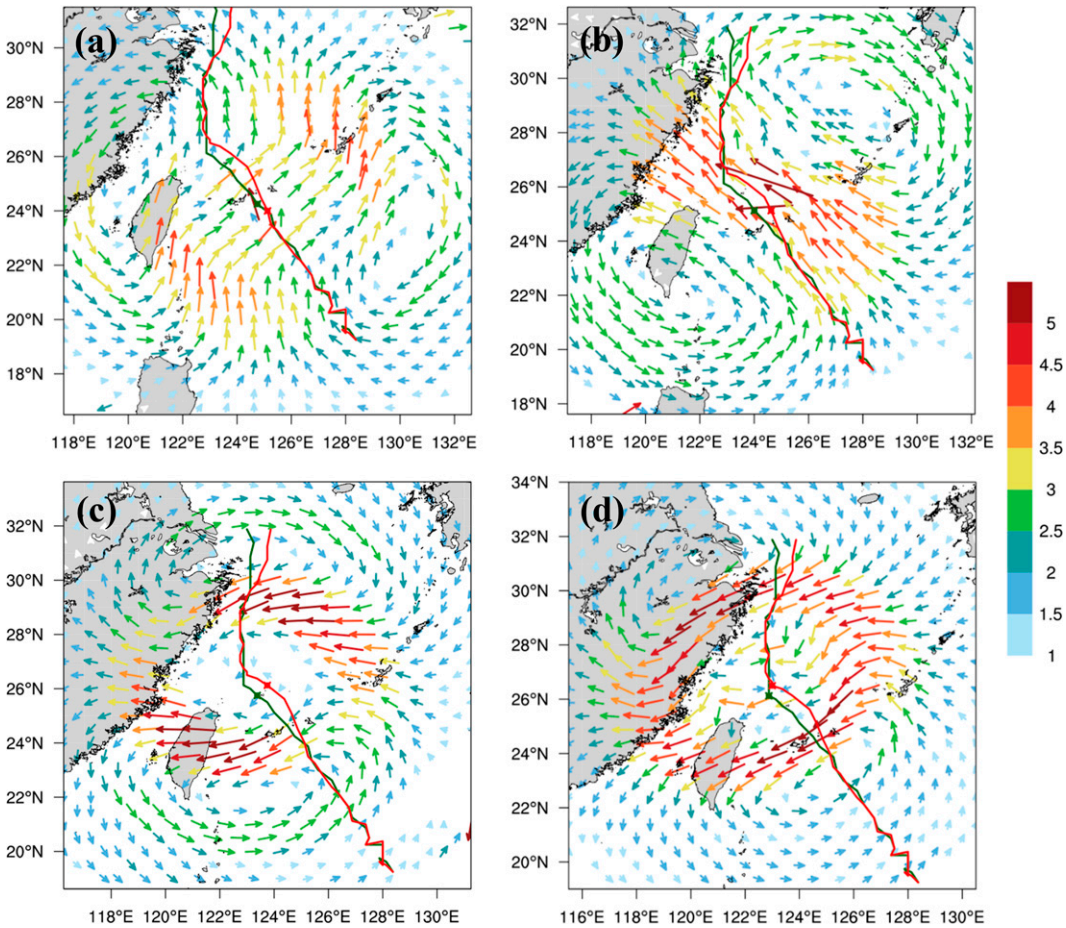

FIG. 12. The wavenumber-1 flow difference (m s^{-1}) averaged for 1–8-km height over the terrain between CTL and noTW at (a) 48, (b) 54, (c) 60, and (d) 66 h. The difference vectors are colored with a scale bar at the right. Red and green lines are the tracks of CTL and noTW, respectively.

the inner eyewall (Fig. 11i). The total of these budget terms indeed provides a similar KE tendency as at 42 h, except with some negative tendency extending outward from the eye in the midtroposphere and positive tendency outside the eyewall in the mid- to upper-tropospheric outer vortex (Fig. 11a). In terms of the mean KE, the vortex after taking the strongest track deflection does not intensify at 54 h as seen from Fig. 3 (the vortex reaches the peak intensity of $V_{\max}$ and MSLP at 51 h). The vortex's weakening in the midtroposphere above 2-km height is mainly owing to the negative work produced by WMRP. Without the Taiwan terrain, WMRP is still very active in producing the KE outside the middle eyewall (Fig. 11j), while WERP has roughly reversed effects near the lower eyewall from CTL (Fig. 11k) and WETP is contrary to WERP at this region (not shown). Outside the radius of 1.5°, there is a reversed negative contribution from WMRP for noTW in 2–4-km height compared to CTL. This indicates that the topographic effects have greatly modified the correlation between the local eddy horizontal velocity and pressure gradient in the inner vortex. The total of these budget terms at 54 h (TTKE) for noTW (Fig. 11l) has less negative KE tendency above about 6-km height in the inner vortex core within 1.5° compared to CTL. The reduced or even reversed correlation between the recirculating flow and the pressure gradient force outside the RMW thus leads to a slight weakening of the typhoon at the later deflection stage in the presence of Taiwan terrain.

f. Track evolution and asymmetric flow

To explain the induced track deflection, Fig. 12 shows the wavenumber-1 (WN-1) flow difference in the horizontal wind averaged in 1–8-km height between CTL and noTW. The flow difference is southerly to the farther south and southeast of the vortex center and becomes southwesterly closer to the inner vortex at 48 h when the track deflection takes place (Fig. 12a). This flow difference indeed is associated with a pair of anticyclonic gyre to the east and cyclonic gyre to the west of the inner vortex. This pair of gyres is rotated counterclockwise toward the northeast with a rather uniform southeasterly flow crossing the inner vortex at 54 h when the vortex is near the strongest deflection (Fig. 12b). The gyre pair keeps

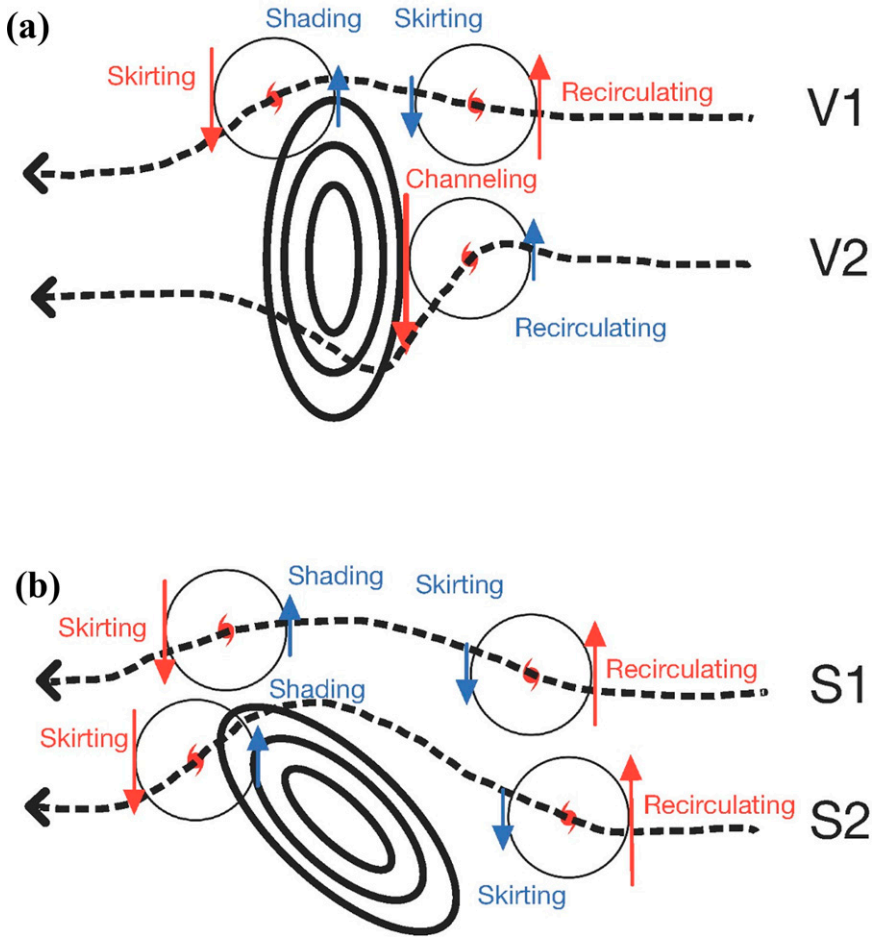

FIG. 13. Schematic diagrams for the vortex track evolution (dashed lines) with flow regime for (a) V-cases (vertical alignment) and (b) S-cases (slant alignment). Solid lines represent the height contours of the bell-shaped mountain (1-km contour interval). Vortex wind intensified by the topographic effect is indicated by larger red vectors, while the weakened one is indicated by smaller blue vectors; the wind change is induced by the flow behaviors of "skirting," "shading," "channeling," and "recirculating," as explained in the text. Terrain contours at an interval of 1000 m are indicated by the black bold lines.

rotating counterclockwise with time as the typhoon is rebounding back in CTL and rejoins the track in noTW (Figs. 12c,d). Such a counterclockwise rotation provides the WN-1 flow difference with more westward-southwestward components in the vicinity of the inner vortex. The formation of a similar rotating gyre pair during the track deflection has also been shown in Tang and Chan (2014) for an idealized northwestward-moving cyclone past the central CMR.

g. *Discussion of contrasting tracks between Maria and Lekima*

The northward track deflection for both Maria and Lekima has been well captured by the high-resolution FV3GFS as shown in our companion paper (Huang et al. 2020b) and this study. Idealized simulations with regional WRF have also helped to identify the track deflection in similarity to the real case of Maria in Huang et al. (2020b). We have also applied the same idealized WRF for Lekima and have identified similar track deflection in numerical experiments.

Figure 13 summarizes the track responses of a translating cyclone moving toward the northward terrain (idealized herein as an elliptical mountain range similar to the CMR) for V-cases (the long mountain axis is oriented northward) and S-cases (the long mountain axis is slanted with a counterclockwise rotation of 50°). For S-cases, the effective mountain length as defined in Fig. 1 is largely reduced as compared to V-cases. The track deflection of Maria is a typical response of V1 with a larger L_D. For V1, slight northward deflection is induced north-northeast of the terrain by the slightly intensified southerly flow component due to the recirculating flow that originates from the splitting flow around the southern corner of the mountain (Huang et al. 2020b). Herein, "recirculating" in the diagram indicates the rejoining flow stemming from the splitting outer vortex circulation around the terrain. After

passing around the northern terrain, the vortex rebounds southward with the stronger skirting flow to the west of the vortex center that is less affected by the terrain and the weaker flow east of the vortex center due to the effect of flow shading by the topographic blocking. "Shading" is used to indicate the departing flow mainly affected by the terrain blocking in the diagram, while "skirting" refers to the incoming flow of the outer vortex toward the terrain.

For V2 (as west-northwestward-moving typhoons approach central Taiwan) with a smaller L_D, a sudden southward deflection is induced ahead of the mountain, possibly due to the intensifying northerly flow arising from effects of flow channeling (e.g., Wu et al. 2015; Huang et al. 2016a, 2020b) or from the wavenumber-1 asymmetry in diabatic heating (Hsu et al. 2018, 2021). Note that a small cyclonic track curvature with northward deflection is indeed induced prior to the strong southward deflection near landfall for such westbound typhoons (e.g., Yeh and Elsberry 1993; Wu et al. 2015; Huang et al. 2016a; Huang and Wu 2018), which is also due to the similar effect of stronger recirculating flow to the east of the inner vortex at the earlier time.

For S1, the vortex track near the terrain is somewhat similar to V1, but with the stronger effect of flow recirculating east of the inner vortex to drive the vortex more northward. With the reduced L_E, the cyclonic track curvature is larger for S1 than V1 as can also be justified by the FV3GFS simulations for both Maria and Lekima. As the effect of the southward skirting flow to the west of the vortex core is dominated by the stronger northward recirculating flow to the east, both S1 and S2 have an apparent northward deflection. This specific type of vortex-terrain configuration influences the behavior of the observed Lekima's track deflection. In response to the largely reduced effective mountain length, L_E, there is no southward deflection for S-cases that can be induced ahead of the mountain base as in V2. This can be attributed to the increased nondimensional number of R/L_E that primarily controls the track deflection of a translating cyclone past the central mountain range (Lin et al. 2005; Huang et al. 2016a).

4. Conclusions

Typhoon Lekima (2019) exhibited a northward track deflection when moving northwestward offshore of northern Taiwan. The northward track deflection of Lekima is stronger and earlier but somewhat similar to that of Maria (2018) with a west-northwestward movement, and the former experienced a rapid intensification prior to and near the track deflection. In this study, we applied the global model FV3GFS to simulate the track and intensity evolution of Lekima prior to and during the offshore passage near northern Taiwan. For improving the simulations, horizontal resolution is enhanced to approximately 7 km by stretching the grids on the face-centered in Taiwan.

The FV3GFS reasonably captures the observed northward track deflection and intensity evolution of Lekima when moving west-northwestward closer to northern Taiwan. The topographic influence of the Central Mountain Range (CMR) in Taiwan causes the northward track deflection of Lekima. The flow splitting around the southern corner of the CMR enhances the southerly radial inflow east of the typhoon vortex that converges with the westerly flow of the inner vortex at the southern flank. Physics sensitivity experiments indicate that similar track deflection can be produced by different cumulus parameterizations when their upstream tracks are similar. The track deflection mechanism has been identified from the physics sensitivity experiments by comparing to their sensitivity experiments without Taiwan terrain. A pair of gyres around the vortex center is exhibited in the difference in the asymmetric wavenumber-1 horizontal wind between the simulations with and without the Taiwan terrain, which is counterclockwise rotating with time to support the evolving deflection direction. The dynamic regime of the observed Lekima's track deflection is essentially similar to the idealized cases as shown in Tang and Chan (2016b) and Huang et al. (2020b).

For Lekima, the increased asymmetric southerly inflow provides the favorable mechanism for northward track deflection but leads to a slightly weakened intensity of the inner vortex core as the deflection is at the strongest stage. The azimuthal mean of KE budget terms in terms of symmetric mean flow and asymmetric eddy parts indicates that the three work rate budget terms related to mean and eddy pressure gradient forces are more important for contributions to KE in the lower-tropospheric vortex. Horizontal (both radial and tangential) and vertical advection of mean and eddy KE provide certain contributions to KE tendency, but with no considerable changes when the Taiwan terrain is removed. In the presence of the Taiwan terrain, however, the positive impacts near the lower eyewall east of Taiwan from the work rate budget terms are weakened due to the reduced or even reversed correlation with the recirculating flow, leading to a slight weakening of the typhoon at the later deflection stage. Negative work rate produced by radial pressure gradient force occur in the middle to upper eyewall outside the RMW associated with the developed radial outflow. However, such topographic effects do not significantly change the intensity of Lekima at later stages of track deflection, due to the fact that the deflecting intense vortex core is still away from the CMR.

The nondimensional number (R/L_y) (R the inner vortex core size and L_y the length scale of the long axis of the mountain range) as proposed by Lin et al. (2005) and Huang et al. (2016a) appears to explain the track deflection of TCs moving toward the central mountain. In this study, we consider the parameters of the effective terrain scale in projection to basic flow (L_E) and the meridional departure of the vortex from the latitude of the mountain peak (L_D). The track responses for incident westbound cyclones at various L_D can be explained by the induced different flow specifications for different L_E. The effective length of the mountain range is reduced so that there is no flow channeling near the mountain base to induce a southward deflection. The observed track defection of Typhoon Lekima appears to be in general agreement with that of an idealized westward cyclone toward the central to northern terrain. With the smaller effective terrain length, the cyclonic track curvature of the northwestbound Lekima is larger than that of the westbound Maria (2018). The simulations add robustness to

the conclusion that minor to moderate terrain-related track deflections can be well simulated by the FV3GFS global model near Taiwan. The roles of L_D and L_E in the track behaviors for more general cyclones moving toward Taiwan will be thoroughly investigated under an idealized framework in the future.

Acknowledgments. This study was supported by the Ministry of Science and Technology (MOST) in Taiwan. We appreciate Dr. D. Nolan for his idealized WRF codes for use. Dr. J.-H. Chen helped provided the computation quota and disk facility at Central Weather Bureau (CWB) for the FV3GFS simulations in this study.

APPENDIX

Formulation of Azimuthal-Mean Kinetic Energy Budget

The governing equations for radial velocity (u) and tangential velocity (v) in cylindrical coordinates (λ, r, z) (λ azimuthal angle, r radius, z height) can be given, respectively, by

$$\frac{\partial u}{\partial t} + u\frac{\partial u}{\partial r} + \frac{v}{r}\frac{\partial u}{\partial \lambda} + w\frac{\partial u}{\partial z} = fv + \frac{v^2}{r} - \frac{1}{\rho}\frac{\partial p}{\partial r} + F_u, \tag{A1}$$

$$\frac{\partial v}{\partial t} + u\frac{\partial v}{\partial r} + \frac{v}{r}\frac{\partial v}{\partial \lambda} + w\frac{\partial v}{\partial z} = -fu - \frac{uv}{r} - \frac{1}{\rho r}\frac{\partial p}{\partial \lambda} + F_v, \tag{A2}$$

where F_u and F_v are turbulent diffusion terms in the boundary layer.

Before deriving the kinetic-energy (KE) equation, we first decompose the variables, $u = \overline{u} + u'$, $v = \overline{v} + v'$, $w = \overline{w} + w'$, $\rho = \overline{\rho} + \rho'$, $p = \overline{p} + p'$ where overbar (prime) is the azimuthal mean (deviation) of a variable in cylindrical coordinates. The local total kinetic energy (TKE), the kinetic energy of azimuthal mean flow (MKE), the local eddy kinetic energy (EKE), and the azimuthal mean of EKE (MEKE) for a tropical cyclone can be defined, respectively, as

$$K = \frac{1}{2}(u^2 + v^2),\ \hat{K} = \frac{1}{2}(\overline{u}^2 + \overline{v}^2),$$
$$K' = \frac{1}{2}(u'^2 + v'^2),\ \overline{K'} = \frac{1}{2}(\overline{u'^2} + \overline{v'^2}).$$

Note that

$$K = \frac{1}{2}(u^2 + v^2) = \frac{1}{2}[(\overline{u} + u')^2 + (\overline{v} + v')^2] = \frac{1}{2}(\overline{u}^2 + \overline{v}^2) + \frac{1}{2}(u^2 + v'^2) + \overline{u}u' + \overline{v}v' = \hat{K} + K' + \overline{u}u' + \overline{v}v'$$

and

$$\overline{K} = \frac{1}{2}(\overline{u^2} + \overline{v^2}) = \frac{1}{2}[\overline{(\overline{u} + u')^2} + \overline{(\overline{v} + v')^2}] = \frac{1}{2}(\overline{u}^2 + \overline{v}^2) + \frac{1}{2}(\overline{u'^2} + \overline{v'^2}) + \overline{\overline{u}u'} + \overline{\overline{v}v'} = \frac{1}{2}(\overline{u}^2 + \overline{v}^2) + \frac{1}{2}(\overline{u'^2} + \overline{v'^2}) = \hat{K} + \overline{K'}.$$

Multiplying (A1) by u and (A2) by v and adding together will give

$$\frac{\partial K}{\partial t} + u\frac{\partial K}{\partial r} + \frac{v}{r}\frac{\partial K}{\partial \lambda} + w\frac{\partial K}{\partial z} = -\frac{u}{\rho}\frac{\partial p}{\partial r} - \frac{v}{\rho r}\frac{\partial p}{\partial \lambda} + uF_u + vF_v, \tag{A3}$$

which describes the tendency of the total kinetic energy. Using the defined KE forms with decomposed azimuthal-mean and asymmetric components, (A3) can be partitioned as

$$\frac{\partial(\hat{K} + K' + \overline{u}u' + \overline{v}v')}{\partial t} + (\overline{u} + u')\frac{\partial(\hat{K} + K' + \overline{u}u' + \overline{v}v')}{\partial r} + \frac{(\overline{v} + v')}{r}\frac{\partial(\hat{K} + K' + \overline{u}u' + \overline{v}v')}{\partial \lambda} + (\overline{w} + w')\frac{\partial(\hat{K} + K' + \overline{u}u' + \overline{v}v')}{\partial z} = -\frac{(\overline{u} + u')}{\rho}\frac{\partial(\overline{p} + p')}{\partial r} - \frac{(\overline{v} + v')}{\rho r}\frac{\partial(\overline{p} + p')}{\partial \lambda} + (\overline{u} + u')(\overline{F}_u + \overline{F}'_u) + (\overline{v} + v')(\overline{F}_v + \overline{F}'_v). \tag{A4}$$

Taking the azimuthal mean of (A4) with the vanishing azimuthal variation gives the budget equation for azimuthal-mean total kinetic energy (MTKE) consisting of 19 terms:

$$\frac{\partial \overline{K}}{\partial t} + \overline{u}\frac{\partial \overline{K}}{\partial r} + \overline{w}\frac{\partial \overline{K}}{\partial z} + \overline{u'\frac{\partial K'}{\partial r}} + \overline{\frac{v'}{r}\frac{\partial K'}{\partial \lambda}} + \overline{w'\frac{\partial K'}{\partial z}} + \overline{u'\frac{\partial(\overline{u}u')}{\partial r}} + \overline{u'\frac{\partial(\overline{v}v')}{\partial r}} + \overline{\frac{v'}{r}\frac{\partial(\overline{u}u')}{\partial \lambda}} + \overline{\frac{v'}{r}\frac{\partial(\overline{v}v')}{\partial \lambda}} + \overline{w'\frac{\partial(\overline{u}u')}{\partial z}} + \overline{w'\frac{\partial(\overline{v}v')}{\partial z}}$$
$$= -\frac{\overline{u}}{\overline{\rho}}\frac{\partial \overline{p}}{\partial r} - \overline{\frac{u'}{\overline{\rho}}\frac{\partial p'}{\partial r}} - \overline{\frac{v'}{\overline{\rho} r}\frac{\partial p'}{\partial \lambda}} + \overline{u}\overline{F}_u + \overline{v}\overline{F}_v + \overline{u'F'_u} + \overline{v'F'_v}, \tag{A5}$$

where the density ρ has been assumed as the azimuthal mean $\overline{\rho}$. The budget terms from the left in (A5) are the time change rate of MTKE (TTKE), mean radial advection of MTKE (RMTKE), mean vertical advection of MTKE (VMTKE), eddy radial advection of EKE (REKE), eddy tangential advection of EKE (TEKE), eddy vertical advection of EKE (VEKE), the energy conversion between the mean flow and eddy including eddy radial advection of weighted radial momentum (ERRM), eddy radial advection of weighted tangential momentum (ERTM), eddy tangential advection of weighted radial momentum (ETRM), eddy tangential advection of weighted tangential momentum (ETTM), eddy vertical advection of weighted radial momentum (EVRM), eddy vertical advection of weighted tangential momentum (EVTM), and the work rates produced by mean radial pressure gradient force (WMRP), eddy radial pressure gradient force (WERP), eddy tangential pressure gradient force (WETP), mean radial friction force (WMRF), mean tangential friction force (WMTF), eddy radial friction force (WERF), and eddy tangential friction force (WETF), respectively. In this study, the asymmetric eddy is the decomposed component in a 200-km radius of the vortex center chosen for the budget analysis. The budget equation in the application here is derived for $\overline{K}$ that includes both $\hat{K}$ and $\overline{K'}$. Different budget forms can also be analyzed for $\hat{K}$ and $\overline{K'}$ (e.g., Wang 2002).

REFERENCES

Black, M. L., and H. E. Willoughby, 1982: The concentric eyewall cycle of Hurricane Gilbert. *Mon. Wea. Rev.*, **120**, 947–957, https://doi.org/10.1175/1520-0493(1992)120<0947:TCECOH>2.0.CO;2.

Chang, C.-P., Y.-T. Yang, and H.-C. Kuo, 2013: Large increasing trend of tropical cyclone rainfall in Taiwan and the roles of terrain. *J. Climate*, **26**, 4138–4147, https://doi.org/10.1175/JCLI-D-12-00463.1.

Chien, F. C., and H. C. Kuo, 2011: On the extreme rainfall of Typhoon Morakot (2009). *J. Geophys. Res.*, **116**, D05104, https://doi.org/10.1029/2010JD015092.

Harris, L. M., S.-J. Lin, and C. Tu, 2016: High-resolution climate simulations using GFDL HiRAM with a stretched global grid. *J. Climate*, **29**, 4293–4314, https://doi.org/10.1175/JCLI-D-15-0389.1.

Hazelton, A. T., L. Harris, and S.-J. Lin, 2018a: Evaluation of tropical cyclone structure forecasts in a high-resolution version of the multiscale GFDL fvGFS model. *Wea. Forecasting*, **33**, 419–442, https://doi.org/10.1175/WAF-D-17-0140.1.

——, M. Bender, M. Morin, L. Harris, and S.-J. Lin, 2018b: 2017 Atlantic hurricane forecasts from a high-resolution version of the GFDL fvGFS model: Evaluation of track, intensity, and structure. *Wea. Forecasting*, **33**, 1317–1337, https://doi.org/10.1175/WAF-D-18-0056.1.

Hsu, L.-H., H.-C. Kuo, and R. G. Fovell, 2013: On the geographic asymmetry of typhoon translation speed across the mountainous island of Taiwan. *J. Atmos. Sci.*, **70**, 1006–1022, https://doi.org/10.1175/JAS-D-12-0173.1.

——, S.-H. Su, R. G. Fovell, and H.-C. Kuo, 2018: On typhoon track deflections near the east coast of Taiwan. *Mon. Wea. Rev.*, **146**, 1495–1510, https://doi.org/10.1175/MWR-D-17-0208.1.

——, ——, and H.-C. Kuo, 2021: A numerical study of the sensitivity of typhoon track and convection structure to cloud microphysics. *J. Geophys. Res. Atmos.*, **126**, e2020JD034390, https://doi.org/10.1029/2020JD034390.

Huang, C.-Y., C.-A. Chen, S.-H. Chen, and D. S. Nolan, 2016a: On the upstream track deflection of tropical cyclones past a mountain range: Idealized experiments. *J. Atmos. Sci.*, **73**, 3157–3180, https://doi.org/10.1175/JAS-D-15-0218.1.

——, I.-H. Wu, and L. Feng, 2016b: A numerical investigation of the convective systems in the vicinity of southern Taiwan associated with Typhoon Fanapi (2010): Formation mechanism of double rainfall peaks. *J. Geophys. Res. Atmos.*, **121**, 12 647–12 676, https://doi.org/10.1002/2016JD025589.

——, C.-H. Huang, and W. C. Skamarock, 2019: Track deflection of Typhoon Nesat (2017) as realized by multiresolution simulations of a global model. *Mon. Wea. Rev.*, **147**, 1593–1613, https://doi.org/10.1175/MWR-D-18-0275.1.

——, C.-W. Chou, S.-H. Chen, and J.-H. Xie, 2020a: Topographic rainfall of tropical cyclones past a mountain range as categorized by idealized simulations. *Wea. Forecasting*, **35**, 20–49, https://doi.org/10.1175/WAF-D-19-0120.1.

——, C.-C. Ruan, H.-C. Kuo, and J.-H. Chen, 2020b: Track deflection of Typhoon Maria (2018) during a westbound passage offshore of northern Taiwan: Topographic influence. *Mon. Wea. Rev.*, **148**, 4519–4544, https://doi.org/10.1175/MWR-D-20-0117.1.

Huang, K.-C., and C.-C. Wu, 2018: The impact of idealized terrain on upstream tropical cyclone track. *J. Atmos. Sci.*, **75**, 3887–3910, https://doi.org/10.1175/JAS-D-18-0099.1.

Huang, Y.-H., C.-C. Wu, and Y. Wang, 2011: The influence of island topography on typhoon track deflection. *Mon. Wea. Rev.*, **139**, 1708–1727, https://doi.org/10.1175/2011MWR3560.1.

Jian, G.-J., and C.-C. Wu, 2008: A numerical study of the track deflection of Supertyphoon Haitang (2005) prior to its landfall in Taiwan. *Mon. Wea. Rev.*, **136**, 598–615, https://doi.org/10.1175/2007MWR2134.1.

Kaplan, J., and M. DeMaria, 2003: Large-scale characteristics of rapidly intensifying tropical cyclones in the North Atlantic basin. *Wea. Forecasting*, **18**, 1093–1108, https://doi.org/10.1175/1520-0434(2003)018<1093:LCORIT>2.0.CO;2.

Lin, Y.-L., and L. C. Savage, 2011: Effects of landfall location and the approach angle of a cyclone vortex encountering a mesoscale mountain range. *J. Atmos. Sci.*, **68**, 2095–2106, https://doi.org/10.1175/2011JAS3720.1.

——, R. D. Farley, and H. D. Orville, 1983: Bulk parameterization of the snow field in a cloud model. *J. Climate Appl. Meteor.*, **22**, 1065–1092, https://doi.org/10.1175/1520-0450(1983)022<1065:BPOTSF>2.0.CO;2.

——, J. Han, D. W. Hamilton, and C.-Y. Huang, 1999: Orographic influence on a drifting cyclone. *J. Atmos. Sci.*, **56**, 534–562, https://doi.org/10.1175/1520-0469(1999)056<0534:OIOADC>2.0.CO;2.

——, D. B. Ensley, S. Chiao, and C.-Y. Huang, 2002: Orographic influences on rainfall and track deflection associated with the passage of a tropical cyclone. *Mon. Wea. Rev.*, **130**, 2929–2950, https://doi.org/10.1175/1520-0493(2002)130<2929:OIORAT>2.0.CO;2.

——, S.-Y. Chen, C. M. Hill, and C.-Y. Huang, 2005: Control parameters for the influence of a mesoscale mountain range on cyclone track continuity and deflection. *J. Atmos. Sci.*, **62**, 1849–1866, https://doi.org/10.1175/JAS3439.1.

——, S.-H. Chen, and L. Liu, 2016: Orographic influence on basic flow and cyclone circulation and their impacts on track deflection of an idealized tropical cyclone. *J. Atmos. Sci.*, **73**, 3951–3974, https://doi.org/10.1175/JAS-D-15-0252.1.

Putman, W. M., and S.-J. Lin, 2007: Finite-volume transport on various cubed-sphere grids. *J. Comput. Phys.*, **227**, 55–78, https://doi.org/10.1016/j.jcp.2007.07.022.

Shi, D., and G. Chen, 2021: Double warm-core structure and potential vorticity diagnosis during the rapid intensification of Supertyphoon Lekima (2019). *J. Atmos. Sci.*, **78**, 2471–2492, https://doi.org/10.1175/JAS-D-20-0383.1.

Tang, C. K., and J. C. L. Chan, 2014: Idealized simulations of the effect of Taiwan and Philippines topographies on tropical cyclone tracks. *Quart. J. Roy. Meteor. Soc.*, **140**, 1578–1589, https://doi.org/10.1002/qj.2240.

——, and ——, 2016a: Idealized simulations of the effect of Taiwan topography on the tracks of tropical cyclones with different sizes. *Quart. J. Roy. Meteor. Soc.*, **142**, 793–804, https://doi.org/10.1002/qj.2681.

——, and ——, 2016b: Idealized simulations of the effect of Taiwan topography on the tracks of tropical cyclones with different steering flow strengths. *Quart. J. Roy. Meteor. Soc.*, **142**, 3211–3221, https://doi.org/10.1002/qj.2902.

Terwey, W. D., and M. T. Montgomery, 2008: Secondary eyewall formation in two idealized, full-physics modeled hurricanes. *J. Geophys. Res.*, **113**, D12112, https://doi.org/10.1029/2007JD008897.

Wang, Y., 2002: Vortex Rossby waves in a numerically simulated tropical cyclone. Part I: Overall structure, potential vorticity, and kinetic energy budgets. *J. Atmos. Sci.*, **59**, 1213–1238, https://doi.org/10.1175/1520-0469(2002)059<1213:VRWIAN>2.0.CO;2.

Willoughby, H. E., J. A. Clos, and M. G. Schoreibah, 1982: Concentric eyewalls, secondary wind maximum, and the evolution of the hurricane vortex. *J. Atmos. Sci.*, **39**, 395–411, https://doi.org/10.1175/1520-0469(1982)039<0395:CEWSWM>2.0.CO;2.

Wu, C.-C., and Y. H. Kuo, 1999: Typhoons affecting Taiwan: Current understanding and future challenges. *Bull. Amer. Meteor. Soc.*, **80**, 67–80, https://doi.org/10.1175/1520-0477(1999)080<0067:TATCUA>2.0.CO;2.

——, T.-H. Li, and Y.-H. Huang, 2015: Influence of mesoscale topography on tropical cyclone tracks: Further examination of the channeling effect. *J. Atmos. Sci.*, **72**, 3032–3050, https://doi.org/10.1175/JAS-D-14-0168.1.

Yeh, T.-C., and R. L. Elsberry, 1993: Interaction of typhoons with the Taiwan topography. Part I: Upstream track deflections. *Mon. Wea. Rev.*, **121**, 3193–3212, https://doi.org/10.1175/1520-0493(1993)121<3193:IOTWTT>2.0.CO;2.

Zhou, L., S.-J. Lin, J.-H. Chen, L. M. Harris, X. Chen, and S. L. Rees, 2019: Toward convective-scale prediction within the next generation global prediction system. *Bull. Amer. Meteor. Soc.*, **100**, 1225–1243, https://doi.org/10.1175/BAMS-D-17-0246.1.